ELSEVIER

Contents lists available at ScienceDirect

# Chemical Engineering Journal

journal homepage: www.elsevier.com/locate/cej





# Photo-excited antibacterial poly( $\mathcal{E}$ -caprolactone)@MoS $_2$ /ZnS hybrid nanofibers

Hui Ci <sup>a</sup>, Lili Ma <sup>a</sup>, Xiangmei Liu <sup>b,\*</sup>, Yanqin Liang <sup>a</sup>, Yufeng Zheng <sup>c</sup>, Zhaoyang Li <sup>a</sup>, Shengli Zhu <sup>a</sup>, Zhenduo Cui <sup>a</sup>, Shuilin Wu <sup>a,c,\*</sup>

- <sup>a</sup> The Key Laboratory of Advanced Ceramics and Machining Technology by the Ministry of Education of China, School of Materials Science & Engineering, Tianjin University, Tianjin 300072, China
- b School of Life Science and Health Engineering, Hebei University of Technology, Xiping Avenue 5340, Beichen District, Tianjin 300401, China
- <sup>c</sup> School of Materials Science & Engineering, Peking University, Beijing 100871, China

#### ARTICLE INFO

Keywords: Antibacterial Nanofiber Heterojunction Photoresponsive Textile

#### ABSTRACT

The rapid and timely sterilization is quite important function for textiles to prevent human being from pathogenic bacterial infections. Hence, it is necessary to develop wearable fabrics with rapid and effective antibacterial properties. In this work, using one-step hydrothermal method and electrospinning, we synthesized biocompatible antibacterial hybrid nanofibers composed of poly(\$\mathcal{E}\$-caprolactone) (PCL) incorporated with heterojunction of MoS2/ZnS (MZ). The MZ endowed the PCL-MZ nanofibers with excellent photothermal and photocatalytic properties under visible light. After 10 min visible light irradiation, the hybrid nanofibers with optimum proportion achieved an effective antibacterial efficacy of 96.03% and 99.09% against <code>Staphylococcus aureus</code> and <code>Secherichia coli</code>, respectively. The underlying mechanism is based on the synergistic effects of reactive oxygen species (ROS) and hyperthermia. Thus, the PCL-MZ hybrid nanofibers will be promising for the fabrication of wearable antibacterial fabrics.

## 1. Introduction

Public health occurrence caused by pathogenic microorganisms has been becoming the forefront of global safety issues [1]. For example, according to Worldometer [2], the current epidemic of COVID-19 is affecting 221 countries and territories, which has caused total infection of over 234.7 million people and over 4.6 million deaths all over the world. The killing and prevention of pathogens are important and necessary for preventing people from infections from these epidemics by using appropriate sterilization methods. Generally, when people wear a properly fitted surgical mask and protective suit, these medical textiles will act as a barrier between the germs and our body. Traditional fabrics can absorb sweat and sebum from human body, as well as stains and oils from the surrounding environment. These substances will provide adequate nutrition for the bacteria attached to the fabrics, promoting them to grow up. Even well-washed fabrics can carry millions of bacteria after just a few hours of wearing, making them an important agent of cross-infection. Consequently, antibacterial fabrics are becoming more and more important in human life, which can conveniently prevent people from bacterial infections and reduce the transmission of bacteria [3]. It has been reported that numerous kinds of materials have excellent antibacterial activity themselves, including Ag-based materials [4–6], metal oxides like Cu<sub>2</sub>O [7,8], and ZnO [9,10], functionalized silicon spheres [11], and organics such as organic quaternary ammonium salts [12,13], N-Halamine [14,15], and chitosan [16,17]. In order to endow fabrics with antibacterial activity, these antibacterial agents were often incorporated into fabrics based on the pad-dry-cure or chemical crosslinking process [11,18,19]. However, the excess solution from the padded procedure during chemical reactions required by these methods is detrimental to the environment [20]. In addition, although these antibacterial agents can kill pathogens, they show toxicity in human body and can even trigger off allergic reaction [8,21]. Therefore, it is necessary to develop effective and simple bacteria-killing strategies, neither inducing pollution to environments nor causing side effects to human body.

Many kinds of emerging strategies have been developed to resist bacterial infections, such as sonodynamic therapy [22,23], microwave-assisted therapy [24-26], phototherapy [27,28], which have drawn

E-mail addresses: liuxiangmei1978@163.com (X. Liu), shuilin.wu@gmail.com (S. Wu).

<sup>\*</sup> Corresponding authors.

wide range of attention due to their rapid and highly-effective antibacterial efficacy without causing bacterial resistance and environmental pollution. Among them, owing to its flexibility and feasibility, phototherapy is suitable and promising for antibacterial fabrics because the photoresponsive materials can be excited to produce antibacterial agents under the irradiation of light with appropriate wavelengths. These photoresponsive materials can absorb the light energy to produce reactive oxygen species (ROS) or/and hyperthermia to kill bacteria within a short time, which will not cause drug-resistance of bacteria [29]. In recent years, many kinds of photoresponsive materials, such as metal nanoparticles [30], metallic oxides [31], transition metal halogenides [32], two-dimensional materials [33], and metal-organic frameworks [34,35], have been developed to kill bacteria by phototherapy. The general mechanism can be summarized into two categories, i.e., photodynamic therapy (PDT) and photothermal therapy (PTT). As for the former, photoresponsive materials can be stimulated to produce electron-hole pairs at specific wavelengths [36], in which some of escaping electrons or holes can be captured by the surrounding oxygen or H<sub>2</sub>O to produce ROS, thus killing bacteria by destroying cell membranes, DNA, and proteins [37–39]. The latter is originated from the interaction between photons and lattice, which causes the lattice vibration and leads to the temperature rise of the materials [40], thereby causing bacteria inactivation. It should be noted that the temperature of PTT needs to be controlled within a reasonable range. If the temperature is too high, it will cause damage to healthy tissues [41].

ZnS is one of the most widely studied photocatalysts due to the rich morphologies, High refractive index, and unique photocatalytic properties [42]. However. Its wide bandgap (3.6 eV) endows this material poor solar harvest with rapid photocarrier recombination. It is a promising to construct ZnS/semiconductor heterojunction to solve these problems. MoS2 is a kind of semiconductor with special physical, optical, and electrical properties because of its ultra-thin atomic layer structure and high specific surface area [43]. Most importantly, the bandgap of this material can be tuned from 1.9 eV to 1.2 eV, by changing the layer thickness. Consequently, MoS2 has a unique light response characteristic from ultraviolet to near-infrared light with a high absorption in the visible part of the solar spectrum. Thereby, it can make up for the low light utilization of ZnS nanoparticles. Poly(&-caprolactone) (PCL) is an aliphatic, semi-crystalline polyester polymer, which has been approved by FDA for pharmaceutical and biomedical use [44]. It is biocompatible [45], biodegradable [46], and nontoxic [47].

Therefore, it is widely used in porous scaffolds [44], nerve regeneration [45,46], and drug delivery systems [48]. In addition, PCL is suitable as a polymer-based matrix because of its high ductility and plasticity in pharmaceutical and packaging applications [49].

Electrospinning is a newly emerging technology that has been extensively used in fabricating ultrathin fibers made of polymers and polymeric composites, which has various applications in wound dressings [50], drug delivery [51], protective clothing [52], and filtration [53]. Electrospun nanofibers are highly porous three-dimensional (3D) network with pore interconnection and have high mechanical strength, large surface area and great flexibility of polymers and composites [53]. Based on the above properties, it is feasible to select an appropriate combination of electrospinning and photoresponsive materials to prepare soft wearable fabrics to achieve a safe and effective antibacterial effect.

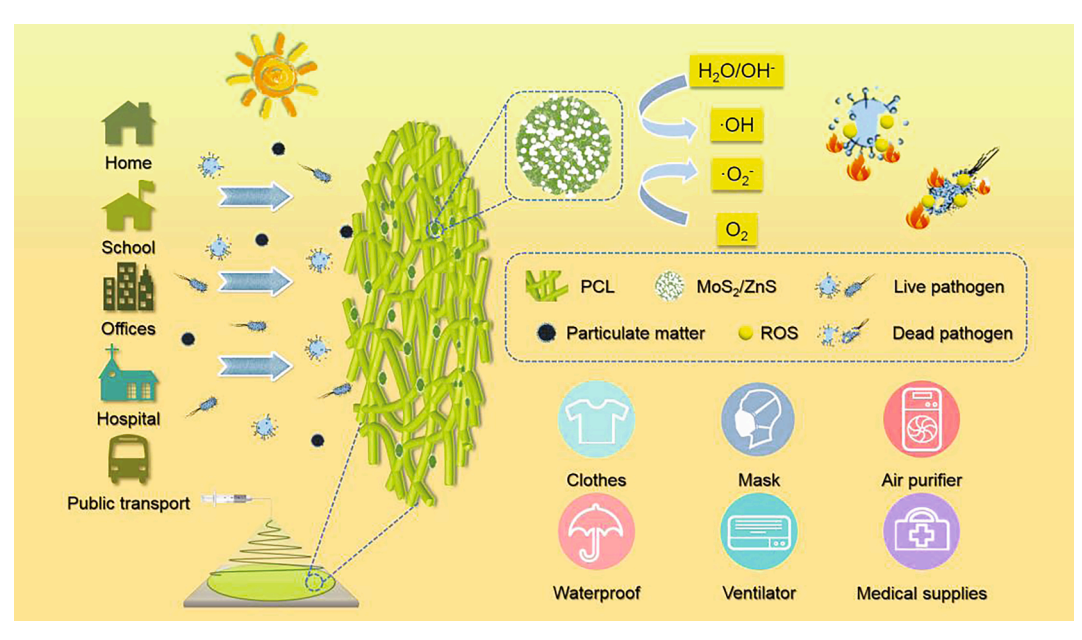
Based on the above-mentioned properties of PCL, ZnS and MoS $_2$ , we proposed a hypothesis whether a biocompatible fabric composed of PCL, ZnS and MoS $_2$  can be prepared by electrospinning, which exhibits highly-effective antibacterial activity within a short time under visible light irradiation.

In this work, as illustrated in Scheme 1, it was reported a flexible and biodegradable PCL nanofiber containing MoS $_2$ /ZnS composites by electrospinning, which could be used to make antibacterial textiles. Briefly, the mixture of polymer and MoS $_2$ /ZnS composites was stretched into nanofibers and deposited into flexible films by an electric field. once the nanofibers were exposed to sunlight, ROS such as  $\cdot O_2^-$  and  $\cdot OH$  was produced and the temperature also increased. The synergistic effect of ROS and high temperature effectively killed the pathogenic bacteria. The PCL-MZ nanofibers had great antibacterial activity, biological safety, and good hydrophobicity.

#### 2. Experimental procedures

#### 2.1. Materials

N, N-Dimethylformamide (DMF, ≥99.9%), thioacetamide ( $C_2H_5NS$ , ≥99.0%) and sodium molybdate dihydrate ( $Na_2MoO_4\cdot 2H_2O$ , >99.0%) were purchased from Aladdin. Tetrahydrofuran (THF, >99.0%) was purchased from Rhawn. Zinc oxide (ZnO, >99.0%) was purchased from Xfnano. Poly( $\mathcal{E}$ -caprolactone) (PCL, M. W 80 000) was purchased from Melun Biological.



Scheme 1. Schematical illustration of PCL-MZ as a combined system for synergistic bacteria-killing by photodynamic and photothermal effects.

#### 2.2. Synthesis of MoS<sub>2</sub>, ZnS, and MoS<sub>2</sub>/ZnS

MoS $_2$ /ZnS heterojunction was synthesized through a simple hydrothermal method. Briefly, 120.98 mg Na $_2$ MoO $_4$ ·2H $_2$ O and 225.39 mg C $_2$ H $_5$ NS were added into 50 mL deionized (DI) water. The mixtures were stirred vigorously for 30 min at 600 rpm and then 97.66 mg ZnO was added with continuously stirring for 15 min at 600 rpm. The mixed solution was transformed into a 100 mL Teflon-lined stainless-steel autoclave. In the next step, the autoclave was heated to 220 °C and maintained for 12 h, and then cooled down to room temperature in the air. The solution in the autoclave was collected and then centrifuged. The obtained powders were washed alternately by DI water and ethanol for several times, and then dried in a vacuum furnace at 60 °C for 6 h to get the powders of MoS $_2$ /ZnS, denoted as MZ. MoS $_2$  and ZnS were synthesized by the above-mentioned hydrothermal process without ZnO or Na $_2$ MoO $_4$ ·2H $_2$ O, respectively.

#### 2.3. Fabrication of PCL-MZ nanofibers

The PCL-MZ nanofibers were fabricated using a conventional electrospinning process. Briefly, the mixed solvent was obtained by stirring THF (4 mL) and DMF (1 mL) for 10 min. The PCL (0.25 g) was dissolved in the above solvent (4 mL) and continuously stirred for 1.5 h at 800 rpm at 30 °C in a water bath to obtain a homogeneous and viscous PCL solution. A desirable amount of MZ nanoparticles (0, 10, 20, 30, 40, or 50 wt% relative to the polymer mass) were dispersed in the mixed solvent (1 mL) and ultrasonicated at 500 W for 1.5 h to obtain MZ suspension. Next, the PCL solution and MZ suspension were mixed with continuously stirring for 8 h at 800 rpm and then fed in a hypodermic syringe (5 mL) before electrospinning. The electrospinning parameters were as follows: electric field strength: 10-12 kV; air gap distance: 15 cm; inner diameter of spinneret: 0.7 mm; flow rate of the solution: 0.015 mL min<sup>-1</sup>; relative humidity: 50-60%, and the electrospinning process was conducted at room temperature. The PCL-MZ nanofibers with the MZ content of 0, 10, 20, 30, and 50 wt% relative to the polymer mass were named as PCL, PCL-10MZ, PCL-20MZ, PCL-30MZ, and PCL-50MZ, respectively. During this process, aluminum foil was used as the collector. All of the membranes were placed under vacuum for 24 h at 25 °C to remove the residual solvent.

# 2.4. Characterization

Both scanning electron microscopy (SEM, s4800, Hitachi) and transmission electron microscope (TEM, JEM-2100F, JEOL) were employed to characterize the morphologies and microstructures of the as-prepared samples. The crystalline structure was analyzed by X-ray power diffraction (XRD, D8 Advanced). The functional groups were determined by a Fourier transform infrared spectrometer (FTIR, Nicolet iS10). Thermal imager (FLIR, E50) was utilized to monitor the temperature variation and obtain the photothermal heating curves of samples. The light absorption of the samples was measured by a UV-2700 optical spectrometer (Shimadu). Simulated sunlight was produced by a Xenon lamp (PLS-SXE300), and the detail information is as follows: the working spot diameter is 30 mm, the parallel light divergence angle is 6°, the maximum output power is 0.3 W cm<sup>-2</sup>, and the irradiation wavelength range is 320–780 nm. The hydrophobicity of the samples was detected by a contact angle instrument (Powereach, JC2000D2).

# 2.5. Photoelectrochemical tests

The photoelectric performances of the synthesized samples were measured in a standard three-electrode cell on CHI660E workstation, in which the Ag/AgCl was the reference electrode, the sample was the working electrode and the platinum network was the auxiliary electrode. The electrolyte was  $0.1~M~Na_2SO_4$  aqueous solution. The photocurrent density was measured in an amperometric i-t mode with a cycle

of 10 s on and 10 s off.

#### 2.6. Detection of ROS

In order to evaluate the photocatalytic performance, the reactive oxygen species (ROS) were detected with 5, 5-Dimethyl-1-pyrroline-Noxide (DMPO) as trapping agent. The reactive species were analyzed by an electron spin resonance spectrometer (ESR, JES-FA200). The samples were dispersed in methanol and DI water, respectively. Next, the above solution was mixed evenly with DMPO. The ESR signals of mixed solution were observed and collected without or with light irradiation for 10 min.

#### 2.7. Antibacterial properties

The antibacterial activity of the as-synthesized samples was evaluated by spread plate counting method. Staphylococcus aureus (S. aureus) and Escherichia coli (E. coli) were used as the experimental strains, which represents the typical Gram-positive bacteria and Gram-negative bacteria, respectively. Before the experiments, all the experimental supplies in the biosafety cabinet were exposed to ultraviolet for 30 min. Then 160 uL of diluted bacterial suspension and 40 uL of samples suspension (ZnS, MoS<sub>2</sub> and MZ, respectively) were added into a 96-well plate, followed by exposure to light irradiation (Xenon lamp, 0.2 W cm<sup>-2</sup>) and dark treatment for 15 min, respectively. The treated bacterial liquids were diluted 100 times. Afterwards, 20 µL of the mixture was evenly spread on an agar plate and placed in a 37 °C incubator. For PCL-MZ nanofiber, the samples were cut into 48-well size, then 80 µL of diluted bacterial suspensions were added into a 48-well plate on the samples, followed by light irradiation (Xenon lamp, 0.2 W cm<sup>-2</sup>) and dark treatment for 10 min, respectively, and 20  $\mu L$  of the mixture was evenly spread on an agar plate and placed in a 37 °C incubator. The antibacterial efficiency was calculated by counting the number of colonies according to the following equation:

Antibacterial ratio (%) = (total bacterial colonies in control group – total bacterial colonies in experimental group) / (total bacterial colonies in control group)  $\times$  100%

# 2.8. Bacterial morphological examination

To better investigate the antibacterial ability of synthesized materials, the morphology of bacteria with or without treatment was determined by SEM. Before the antibacterial assay, the plates were placed in a 48-well plate, after light irradiation in the antibacterial experiment, the mixed bacteria solution in 48-well plate was allowed to stand for 2 h to allow the bacteria to adhere to the plates. The bacteria were fixed with 2.5% glutaraldehyde for 40 min, and then dehydrated by ethanol solutions with increasing concentrations (30%, 50%, 70%, 90% and 100%) for 20 min successively. The plates dried at 4 °C were sprayed with gold and observed by SEM.

#### 2.9. Cytotoxicity assay

Using NIH-3 T3 (Mouse fibroblasts) as experimental cells, the cytotoxicity of the synthesized samples was evaluated by Thiazolyl Blue Tetrazolium Bromide (MTT) test. First, the cells were seeded in 48-well plates and cultured in a 95% carbon dioxide incubator at 37  $^{\circ}\text{C}$  for 24 h. Different samples were put in wells for light illumination and dark treatments. After incubation, MTT solution was put in the wells after aspirating the liquid, and then the plates were kept in an oven at 37  $^{\circ}\text{C}$ . Next, the MTT solution was discarded, and then dimethyl sulfoxide (DMSO) was added into the wells followed by shaking for 10 min on a shaker. At last, a microplate reader was utilized to measure the optical density of the supernatant liquid at 490 nm.

Cell viability (%) = (OD value of experimental group) / (OD value of control group)  $\times$  100%

#### 2.10. Statistical analysis

All experimental data are shown as mean with standard deviation (S. D.). The statistical method was mainly t-test. The experiments were repeated for at least 3 times. When the p-value was<0.05, it was believed statistically significant.

#### 3. Results and discussion

# 3.1. Characterization of PCL-MZ

The morphologies of synthesized materials were shown in Figure S1 (Supporting information). The size of ZnO used in the experiment was about 20 nm (Fig. S2A). The average size of pure ZnS prepared by hydrothermal method was about 65 nm, which was larger than that of ZnO (Fig. S2B). Petal-like MoS<sub>2</sub> particles were in different sizes and made up of stacked multiple layered structures (Fig. S1C). According to Fig. S1D, the surface of MZ was composed of many uniformly sized particles that might be ZnS. The average size of ZnS formed on the surface of MZ was about 32 nm, smaller than pure ZnS (Fig. S2C). It indicated that the insitu generation of MoS<sub>2</sub> was beneficial to control the growth of ZnS particles and could make them more uniform and smaller in size. The phase compositions of the synthesized MZ were characterized by XRD. XRD pattern (Fig. 1A) disclosed the formation of ZnS, which was attributed to the chemical reaction between ZnO and H2S produced from C<sub>2</sub>H<sub>5</sub>NS in the hydrothermal process as the following equations (Eq. (1) and (2)):

$$C_2H_5NS + H_2O \rightarrow C_2H_5NO + H_2S \tag{1}$$

$$ZnO + H_2S \rightarrow H_2O + ZnS$$
 (2)

No ZnO peaks were observed according to the above reactions. The weak diffraction peaks of MoS2 in the XRD patterns of MZ composites could be observed. It indicated that MZ was composed of ZnS and MoS<sub>2</sub> instead of ZnO. TEM analysis was performed to investigate the nanosized heterostructures in Fig. 1B-E. As shown in Fig. 1B, MZ was constituted by abundant nanosheets and nanoparticles of about 30 nm. It was similar to the results of SEM. High-resolution transmission electron microscopy (HRTEM) characterization was conducted as shown in Fig. 1C. The lattice spacing of 0.27 nm indicated the (100) facet of MoS<sub>2</sub> and 0.33 nm specified the (111) facet of ZnS, providing the existence of MoS<sub>2</sub> and ZnS. The selected area electron diffraction (SAED) image (Fig. 1D) indicated that MZ composites were composed of polycrystalline ZnS and hexagonal MoS2, consistent with XRD patterns. The EDS mapping of Mo, S, Zn, and O was showed in Fig. 1E. Mo, O and S were uniformly distributed throughout the detection area, while Zn was localized, which suggested the existence of ZnS. Fig. 1F shows the atomic structure of the MZ heterojunction. ZnS had a weak positive potential of about 3.17 mV, while MoS2 exhibited a negative potential of about -49.42 mV (Fig. 1G). The negative potential of MZ was about -27.97 mV, which is more positive than MoS<sub>2</sub>.

Fig. 2 displays the XPS of ZnS, MoS<sub>2</sub>, and MZ, revealing the chemical compositions and interactive information. XPS survey spectra show the existence of Zn, Mo, and S in the samples. In Fig. 2B, two major Zn 2p

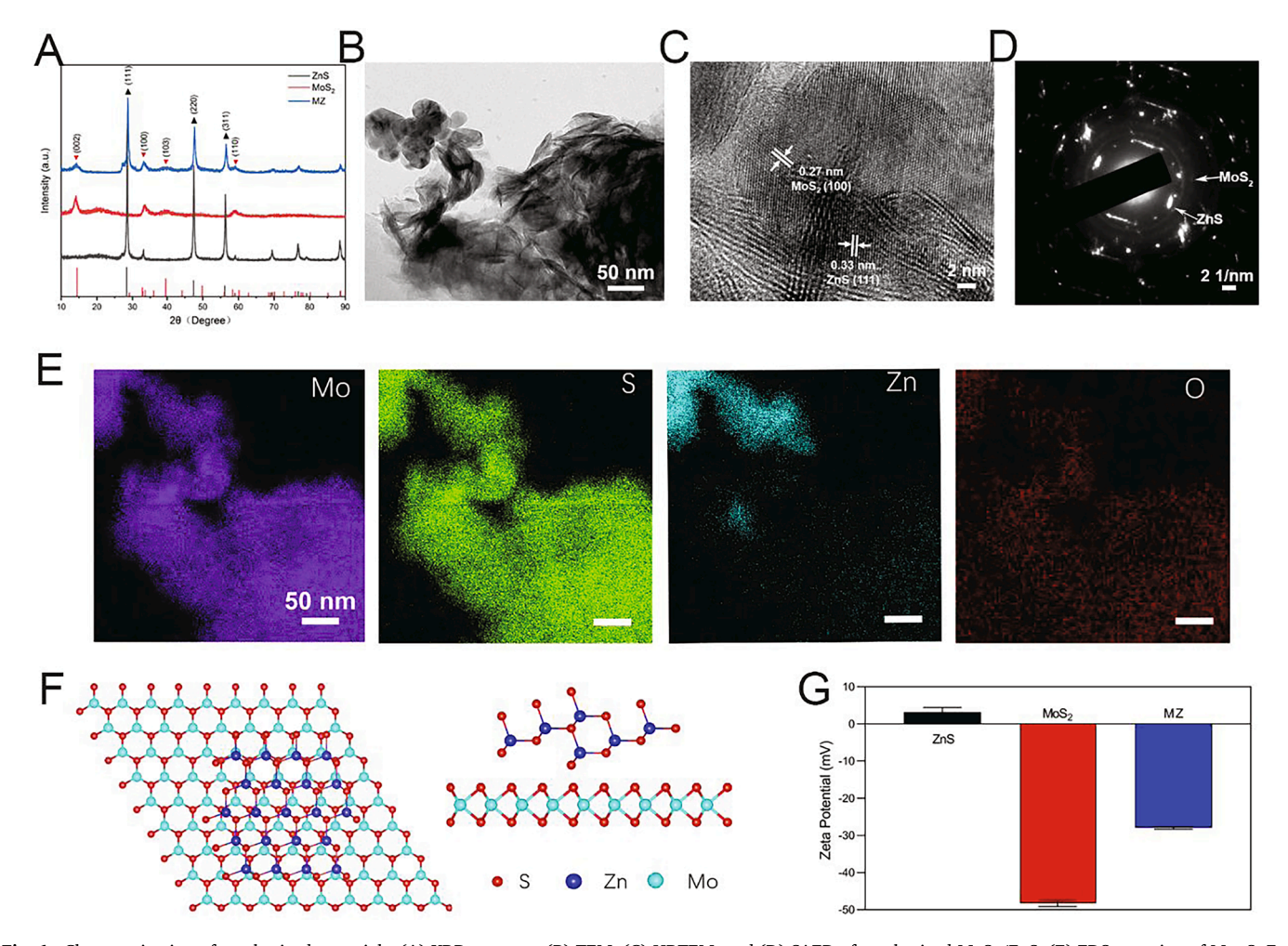


Fig. 1. Characterization of synthesized materials. (A) XRD patterns, (B) TEM, (C) HRTEM, and (D) SAED of synthesized MoS<sub>2</sub>/ZnS, (E) EDS mapping of Mo, S, Zn, and O in synthesized MoS<sub>2</sub>/ZnS shown in (B), (F) Structure, (G) Zeta potential.

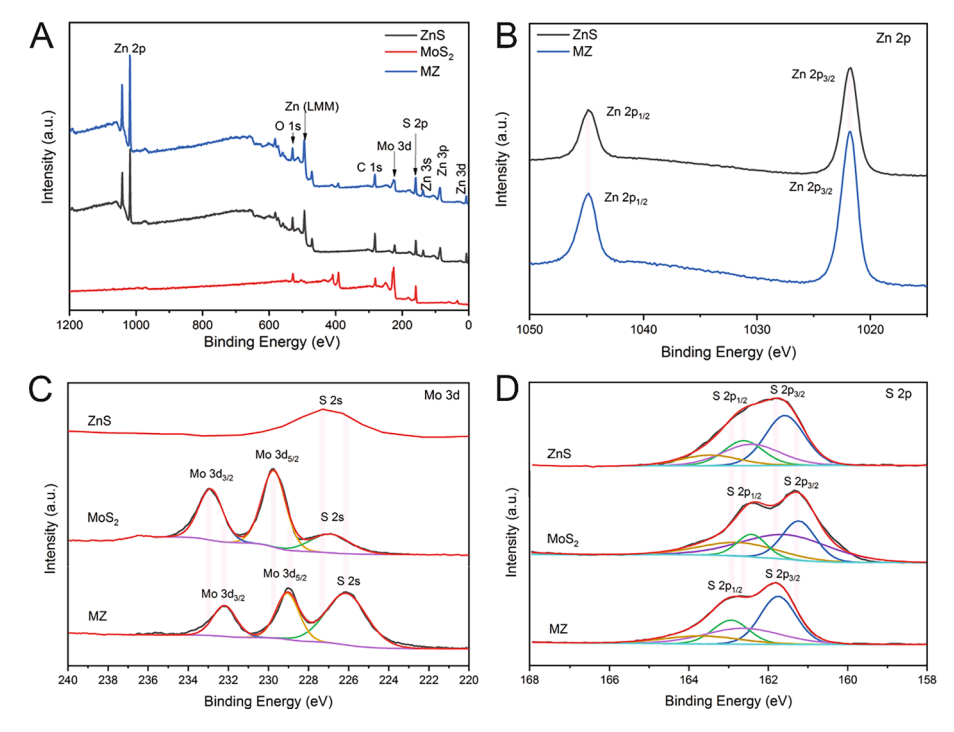


Fig. 2. (A) XPS survey spectra of ZnS, MoS<sub>2</sub>, and MoS<sub>2</sub>/ZnS. The XPS narrow scan of (B) Zn 2p, (C) Mo 3d, and (D) S 2p.

peaks of ZnS were located at 1021.71 eV and 1044.81 eV, corresponding to Zn  $2p_{3/2}$  and Zn  $2p_{1/2}$ , respectively. The two Zn 2p peaks of MZ were located at 1021.84 eV and 1044.94 eV, respectively. The Zn 2p peaks of MZ were shifted compared to that of ZnS. The results demonstrated that there was a surface binding interaction between ZnS and MoS2, promoting the separation of photogenerated charges [54]. The peaks of Mo  $3d_{5/2}$  and Mo  $3d_{3/2}$  (Fig. 2C) were located at 229.78 eV and 232.92 eV, respectively, consistent with the Mo<sup>4+</sup> of pure MoS<sub>2</sub>; while for MZ, these two peaks were located at 229.20 eV and 232.34 eV, which might be due to the discontinuous growth of nanosheets after coupling with ZnS. S 2p spectrum shown in Fig .2D was studied to investigate the interaction between ZnS and MoS2. The peaks observed at 161.77 eV and 162.68 eV were consistent with the S<sup>2-</sup> of ZnS, while the peaks at 161.31 eV and 162.47 eV were assigned to MoS2. S 2p peaks of MZ had a slight shift compared to ZnS and MoS2, which was caused by partial electron transfer from ZnS to MoS2.

The SEM images of PCL nanofibers incorporated with different amounts of MZ were shown in Fig. 3A-D. Pure PCL nanofibers were smooth, with white appearance, as seen from Fig. 3A. With the increasing of MZ content in the precursor dispersion, the particle amount in the nanofibers proportionally increased and the color became dark. Most of the MZ particles were wrapped or semi-wrapped in PCL nanofibers, and there were some particles between PCL nanofibers. This structure might facilitate the release of ROS, thus improving the sterilization efficacy. The XRD patterns of PCL-MZ with different weight ratio of MZ were shown in Fig. 3E. The major diffraction peaks located between 20° and 25° were attributed to PCL, and the intensity of characteristic peaks of MZ were enhanced gradually with the increase of MZ incorporated ratio, and these peaks could be obviously seen in PCL-30MZ. This result again confirmed the existence of MZ in PCL nanofibers. FT-IR studies for PCL, PCL-10MZ, PCL-20MZ, and PCL-30MZ nanofibers were further performed to study the functional group in Fig. 3F. The typical bands for PCL could be observed, and it demonstrated the addition of MZ did not affect the structure of PCL.

# 3.2. Photothermal and photodynamic properties

As MoS<sub>2</sub> has excellent photothermal ability with full-spectrum

absorption, it is presumed that MoS2 in MZ composites can also generate heat under continuous irradiation of simulated sunlight. As shown in Fig. S3, the temperature elevation increased with increasing the concentration of MZ composites. And MZ composites had good photothermal conversion behavior at 500 μg mL<sup>-1</sup> after irradiating for 15 min. In order to prove that the PCL-MZ nanofibers still retain good photothermal performance after the electrospinning process, PCL-MZ with different MZ ratios was tested by a Xenon lamp. As shown in Fig. 4A and B, pure PCL exhibited negligible photothermal property under irradiation of simulated sunlight. With the addition of MZ composites, the photothermal response of the membranes was significantly improved. The photothermal stability of PCL-30MZ was measured by the photothermal response cycling test in Fig. 4C. Under on-off irradiation conditions, the temperature of PCL-30MZ exhibited a stable on-off effect, indicating the excellent photothermal stability of PCL-30MZ. The samples arranged from right to left in Fig. 4D were PCL, PCL-10MZ, PCL-20MZ, PCL-30MZ, and black PCL, respectively. The black PCL was obtained by dyeing pure PCL with black dye and served as a control. The actual sunlight intensity was measured to be 0.036 W cm<sup>-2</sup>. After being exposed to the sun for 10 min, the temperature of PCL, PCL-10MZ, PCL-20MZ, PCL-30MZ, and black PCL were 37.9 °C, 40.0 °C, 42.4 °C, 42.5 °C, and 43.0 °C, respectively. The samples were then immediately placed in dark conditions. The temperature difference of PCL-20MZ and PCL-30MZ were smaller than that of other samples. At the same time, the temperature of PCL-20MZ and PCL-30MZ were 0.6-1.9 °C higher than other samples. The experimental results proved that the PCL-30MZ nanofibers could meet the heat preservation requirements of everyday wear in daylight.

The light absorption spectra of PCL-MZ nanofibers were shown in Fig. 4E. Compared to pure PCL, PCL-MZ not only has broadened absorption spectra, but also further enhanced the absorption capability of light after the incorporation of MZ composites. As PDT and PTT synergistic therapy is much better than a single one, PCL-30MZ, which has the best photothermal effect, was taken as an example to determine  $\cdot O_2^-$  and  $\cdot$  OH generated in the PDT process [34]. When PDT and PTT are combined, ROS can increase the permeability and thermal sensitivity of bacterial membranes, while membrane permeability can also be increased in higher temperature, thereby strengthening the therapeutic

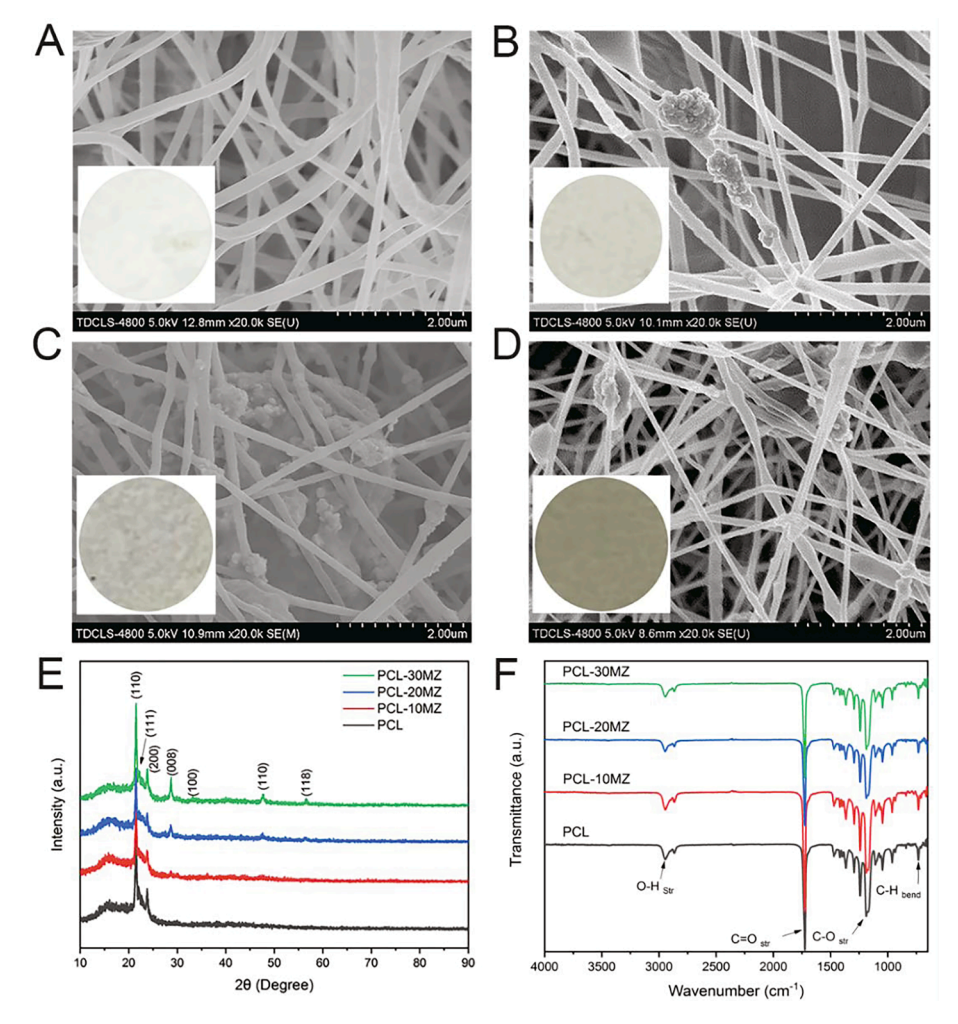


Fig. 3. Morphologies of synthesized nanofibers. SEM images of (A) PCL, (B) PCL-10MZ, (C) PCL-20MZ, (D) PCL-30MZ, and insets show the optical photographs of the nanofibers. (E) XRD pattern; (F) FT-IR spectra.

effect of ROS by accelerating the leakage of proteins and other ingredients from bacteria [29]. As shown in Fig. 4F and G, there were no ESR signals detected in dark, suggesting the ROS could not be generated without light. Whereas, after light irradiation for 10 min, the weak four-line peaks appeared (Fig. 4F), which were indexed to DMPO-  $\cdot$ O<sub>2</sub><sup>-</sup> adducts. At the same time, the characteristic peaks of DMPO-  $\cdot$ OH adducts with an intensity ratio of 1:2:2:1 were detected by ESR (Fig. 4G), indicating that PCL-30MZ can effectively produce  $\cdot$ O<sub>2</sub><sup>-</sup> and  $\cdot$ OH species under illumination. ESR signals of  $^{1}$ O<sub>2</sub> (Fig. S4) and H<sub>2</sub>O<sub>2</sub> detection (Fig. S5) of PCL-30MZ showed that only  $\cdot$ O<sub>2</sub><sup>-</sup> and  $\cdot$ OH were produced.

In this work, the energy gap of ZnS,  $MoS_2$ , and MZ was 3.6 eV, 1.2 eV, and 0.62 eV, respectively (Fig. S6). Meanwhile, the potential values of conduction band (CB) and valence band (VB) of photocatalysts can be calculated according to Eq. (3) and (4) [55].

$$E_{VB} = \chi - E_e + 0.5E_g \tag{3}$$

$$E_{CB} = E_{VB} - E_g \tag{4}$$

In which  $\chi$  means the electronegativity of the semiconductor, and  $E_e$  is the energy of free electrons with a value of 4.5 eV ( $\nu s$  NHE). From the above, the calculated CB and VB potential of ZnS and MoS $_2$  were -1.04 eV, -0.51 eV, and 2.56 eV, 0.69 eV  $\nu s$  NHE, respectively. The photoelectrochemical performance is displayed in Fig. 5 to investigate the photogenerated charges transfer and recombination of ZnS, MoS $_2$ , and MZ. Under the same conditions, the transient photocurrent response of MZ was higher than that of ZnS and MoS $_2$  (Fig. 5A). The Nyquist plots of

electrochemical impedance spectroscopy (EIS) represented a smallest radius of MZ, revealing a fastest photogenerated charge separation and transfer efficiency in it (Fig. 5B). Fig. S7 showed the current density of PCL-30MZ. These phenomena showed that the composition of ZnS and MoS<sub>2</sub> improved the photocatalytic performance and enhanced the separation of photoelectron-hole pairs. Meanwhile, the *in situ* generated ZnS was located on the surface of MZ, thus more photogenerated charge transfer interfaces were formed, which suppressed the recombination of electron-hole pairs [56]. Hence, the photocatalytic efficiency was improved.

Fig. 6 gives a schematic illustration of the possible photocatalytic and photothermal mechanisms. MZ was a typical  $\it{I}$ -type, as shown in the energy diagram. Under light irradiation, the electrons in the VB of ZnS was excited to CB, leaving a hole in VB. Compared to ZnS, MoS $_2$  had a more negative CB and a more positive VB. Hence, the electrons and holes were drawn to the CB and VB of MoS $_2$ , respectively. Thus, the separation of photoinduced charge carriers was improved compared to that in ZnS alone, and the photodegradation process was enhanced in the nanocomposite. There may also be a structural mismatch between ZnS and MoS $_2$ , resulting in more time for carriers to travel through the heterogeneous interface. Hence, the electrons and holes can react with surrounding O $_2$  and H $_2$ O/OH $_1$  to produce  $_2$ 0 $_1$ 1 and  $_2$ 1 oH, respectively, which is detrimental to bacteria. Moreover, the photothermal effect of MoS $_2$ 2 was also triggered by light irradiation. Consequently, ROS and heat generated from MZ worked together, synergistically killing bacteria.

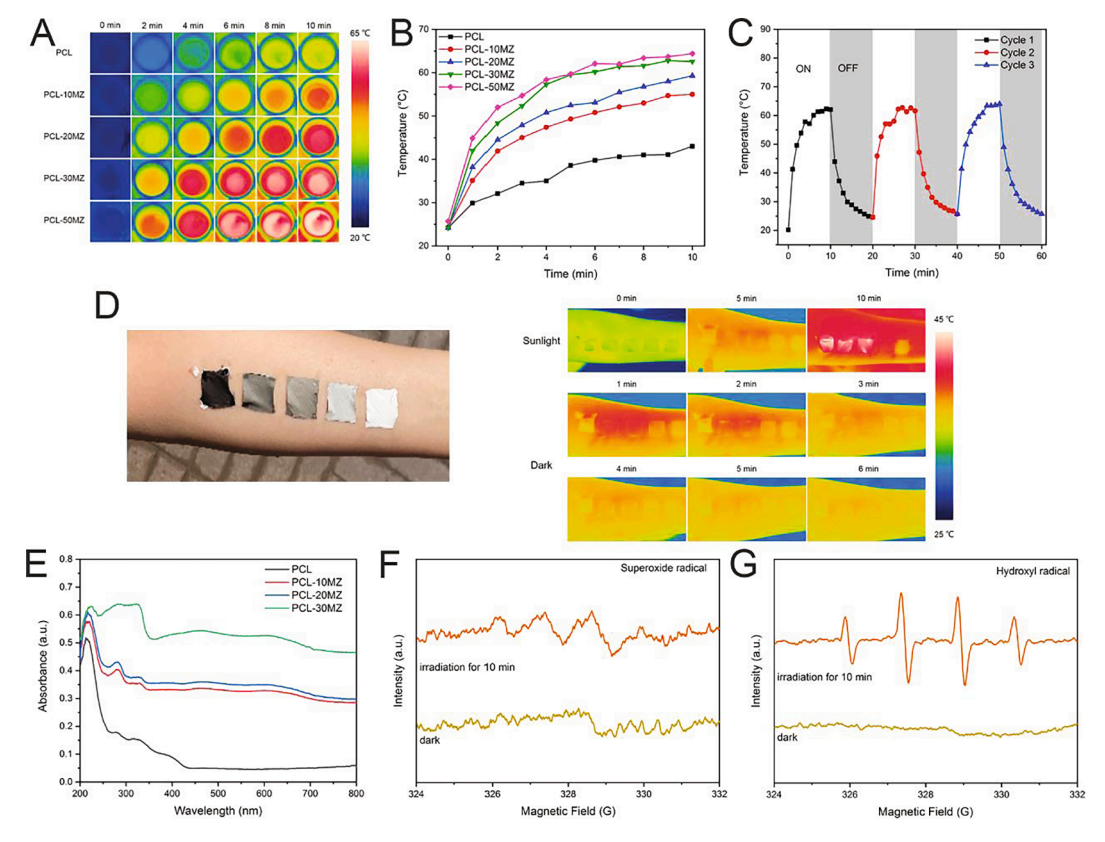


Fig. 4. Photothermal and photodynamic effects of samples under light irradiation for 10 min. (A) Infrared thermal images. (B) Photothermal heating curves of PCL, PCL-10MZ, PCL-20MZ, PCL-30MZ, PCL-30MZ, PCL-50MZ, 0.2 W·cm<sup>-2</sup>. (C) Temperature rising and cooling profiles of PCL-30MZ with 3 cycles of light on–off and the following cooling, 0.2 W·cm<sup>-2</sup>. (D) Optical photographs of different PCL-MZ nanofibers on the arm and the corresponding infrared thermal images. (E) UV-vis-NIR spectra of PCL, PCL-10MZ, PCL-20MZ and PCL-30MZ. ESR spectra of (F) ·O<sub>2</sub> by DMPO-, and (G) •OH by DMPO- obtained from PCL-30MZ before and after 10 min light irradiation.

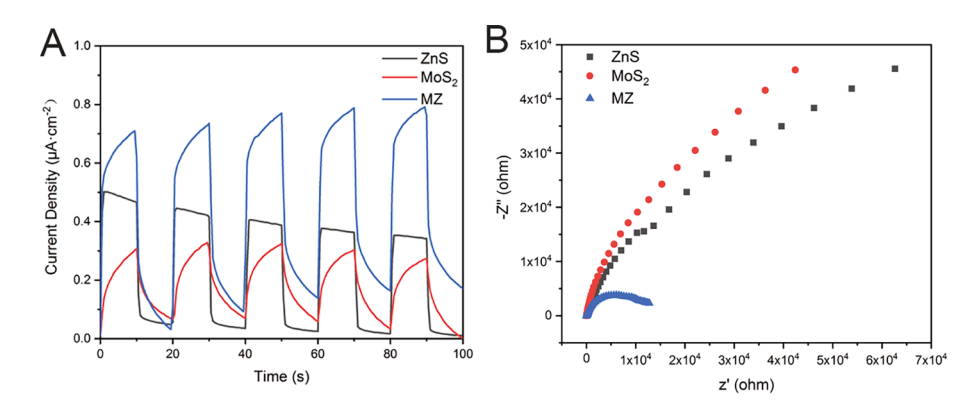


Fig. 5. Photoelectrical properties of synthesized samples under light irradiation. (A) Photocurrent density. (B) EIS spectra.

#### 3.3. Antibacterial ability

The antibacterial properties of MZ composites and PCL-MZ nanofibers were tested respectively. According to the number of colonies shown in Fig. S8, MZ composites exhibited better antibacterial performance than individual ZnS and MoS<sub>2</sub>. The antibacterial ability of PCL-MZ nanofibers was evaluated against *S. aureus* and *E. coli in vitro* by plate counting method as shown in Fig. 7. The antibacterial ability of PCL-MZ nanofibers was endowed by MZ composites, while pure PCL could not effectively kill bacteria under light stimulation. The antibacterial ratios of 10%, 20%, and 30% PCL-MZ nanofibers went up to 63.73%, 84.08% and 96.03% against *S. aureus* (Fig. 7A, B) and 52.52%, 88.78% and 99.09% against *E. coli* (Fig. 7C, D) under light irradiation,

respectively. Obviously, with the increase of MZ composites content, the antibacterial efficiency of the nanofibers increased continuously. Antibacterial efficiency of PCL-30MZ (Fig. S9) was similar to that of PCL-30MZ, but the spinnability of PCL-50MZ was much worse. The antibacterial efficacy of PCL-30MZ after different time of illumination was shown in Fig. S10, and it was significantly increased after irradiation for 2 min, consistent with the photothermal heating curve in Fig. 4B. Compared with the MZ composites, the antibacterial properties of the PCL-MZ nanofibers had not been diminished at all, even if the irradiation time was shortened. The antibacterial cycle experiments (Fig. S11) demonstrated that the nanofibers could maintain excellent antibacterial efficacy after repeated washing.

To further elucidate the antibacterial behavior, the morphology and

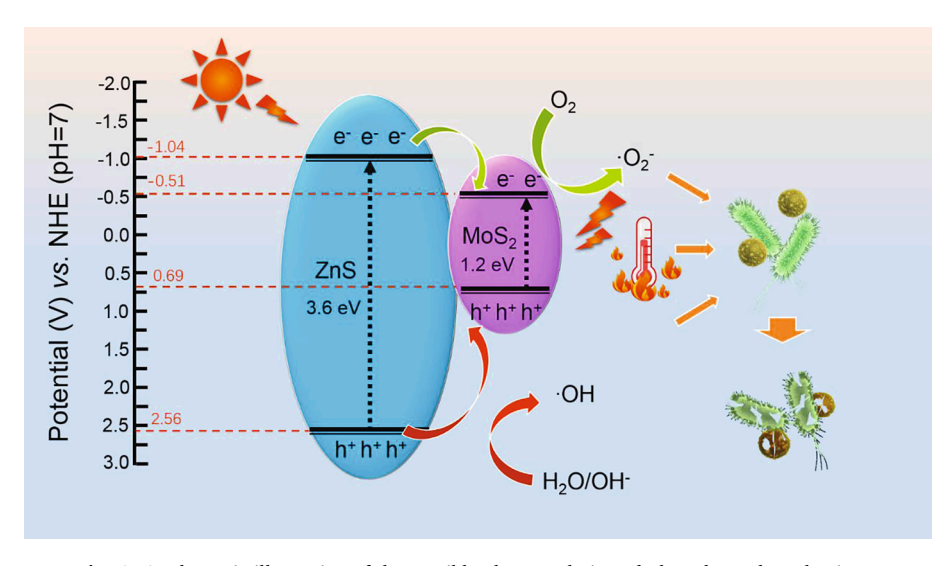
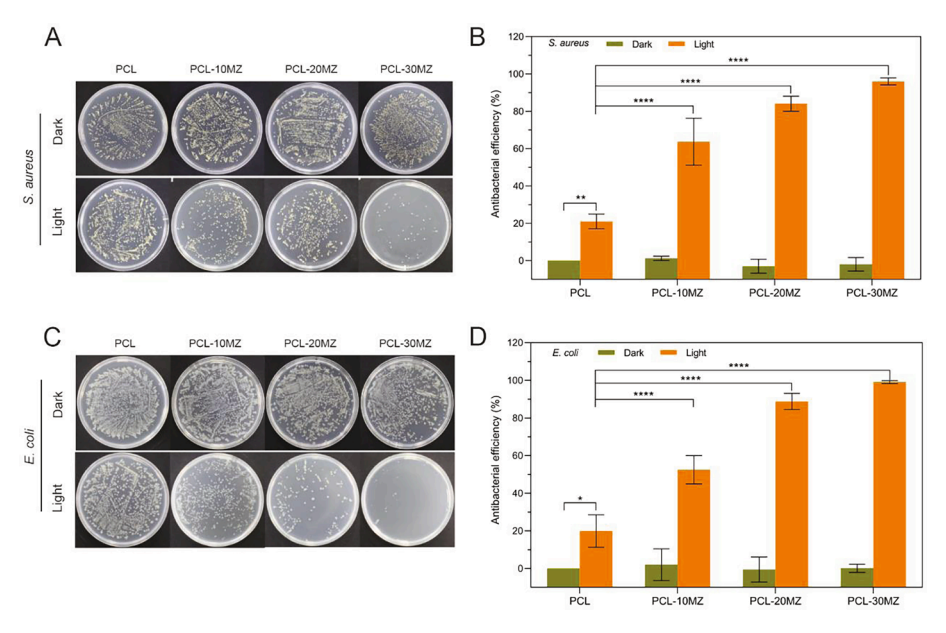


Fig. 6. A schematic illustration of the possible photocatalytic and photothermal mechanisms.



**Fig. 7.** In vitro antibacterial assay showing the spread plate results and the histograms of the antibacterial efficiency of (A, B) S. aureus and (C, D) E. coli. The bacteria were mixed with the membranes, then exposed to simulated sunlight or kept in dark for 10 min, and then spread onto LB agar plate and incubated at 37 °C for 24 h. The error bars indicate means  $\pm$  SD (n = 3): \*p < 0.05, \*\*p < 0.01, \*\*\*\*p < 0.001, \*\*\*\*p < 0.0001.

membrane integrity of bacteria treated with all samples with or without light irradiation were observed by SEM. As shown in Fig. 8A, after being treated with PCL, PCL-10MZ, PCL-20MZ, and PCL-30MZ in the dark, S. aureus maintained a complete and smooth shape. After irradiated by sunlight for 10 min, the nanofibers mixed with MZ composites depressed the surface of S. aureus and then deactivated it. The cell membrane of S. aureus became rough and wrinkled, or even ruptured. Similarly, a few disruptions occurred on the cell walls on the rod-shaped E. coli as well (Fig. 8B). The distortion and rupture of bacteria membranes were worse with the increase of MZ content in fabrics, which was consistent with the plate counting results. Protein leakage measurement (Fig. S12) proved that MZ destroyed the cell membrane of bacteria to sterilize, supporting the results of Fig. 8. Among those PCL-MZ nanofibers, PCL-30MZ exhibited the best antibacterial efficacy, which was ascribed synergetic combination between moderate photothermal temperature and proper photocatalytic activity. The photothermal property from MoS<sub>2</sub> has a continuous heating effect on the bacteria, which can change the permeability of the bacterial cell membrane and denature the enzymes

and other proteins. It makes up for the transient lifetime (<40 ns) and short diffusion distance (approximately 10 nm) of ROS, and encourages ROS to contact with or even enter bacteria [29,57]. ROS produced by MZ heterojunction can also increase the permeability and thermal sensitivity of damaged bacterial membranes. These two therapies complemented each other and achieved synergistic effects on killing bacteria. Antibacterial experiment (Fig. S13) with only high temperature or ROS well confirmed this conclusion.

#### 3.4. Biocompatibility

The cell response of different samples *in vitro* was used to evaluate the cytotoxicity of the as-synthesized fiber membranes. As shown in Fig. 9A, all cells co-cultivated with PCL-MZ nanofibers for one day showed a slight increase in cell viability without light, indicating that the PCL-MZ nanofibers were ecofriendly. The more content of MZ in PCL-MZ, the more cells were alive, proving the excellent biosafety of the nanofibers. After three days of culture, the cell viability of PCL-MZ was

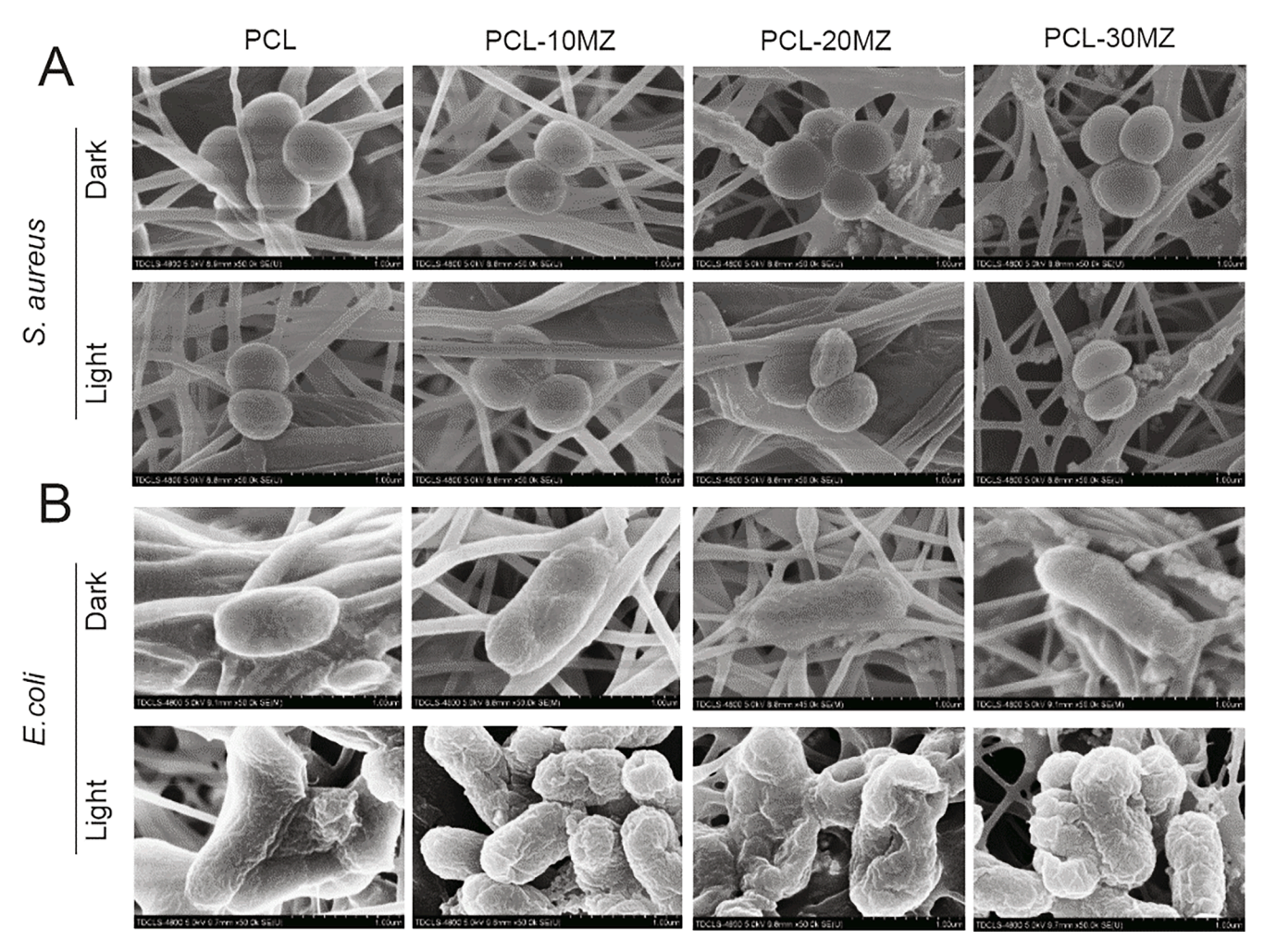
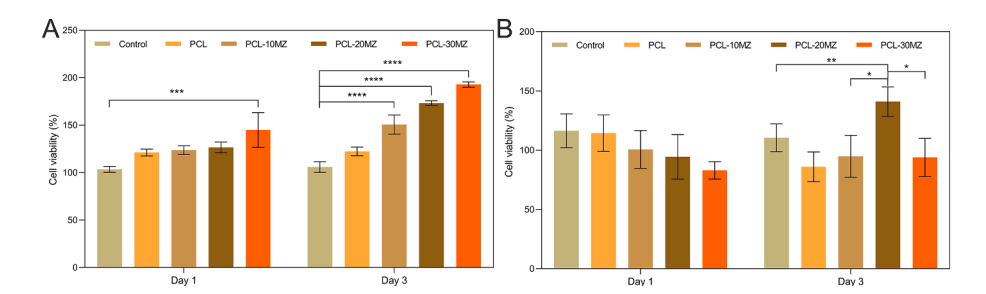


Fig. 8. The morphologies and structures of (A) S. aureus and (B) E. coli after irradiation or dark treatment for 10 min.



**Fig. 9.** MTT assay of cell viabilities cultured in the medium with different samples after co-culture for 1 day and 3 days. (A) In the dark, (B) Under light. The error bars indicate means  $\pm$  SD (n = 3): \*p < 0.05, \*\*p < 0.01, \*\*\*\*p < 0.001, \*\*\*\*p < 0.0001.

still higher than that of the control. It was observed that the number of surviving cells increased on the third day. To explore the effect of light on organism, cells and PCL-MZ nanofibers were co-cultured for one and three days after 10 min of light, respectively (Fig. 9B). Cells irradiated with light showed less activity than those in the dark group, maybe due to high temperature. However, it could still be>75% cell viability in light group. Cells cultured with PCL-20MZ for three days had the highest viability, indicating the best biocompatibility. Compared with the studies of Wang [58], Yasaman Ghiyasi [59], and Liu [60] et al., PCL-MZ nanofibers can kill bacteria efficiently and quickly in a short time with great biological safety.

To detect the difference in the hydrophobicity before and after the addition of MZ composites, water contact angles were examined. In

Fig. 10, the water contact angle of the pure PCL was 109.33°, while for PCL-10MZ, PCL-20MZ, and PCL-30MZ, the water contact angles were 130.58°, 131.25°, and 131.92°, respectively. It was obvious that the hydrophobicity of PCL was improved after adding MZ. With the increase of MZ content, the hydrophobicity of PCL-MZ also increased correspondingly, but the change was not significant. In addition, PCL-MZ nanofibers had good air permeability (Fig. S14), making them suitable for fabrics.

## 4. Conclusions

In summary, MoS<sub>2</sub>/ZnS heterojunctions were successfully fabricated through a facile hydrothermal approach and prepared PCL-based

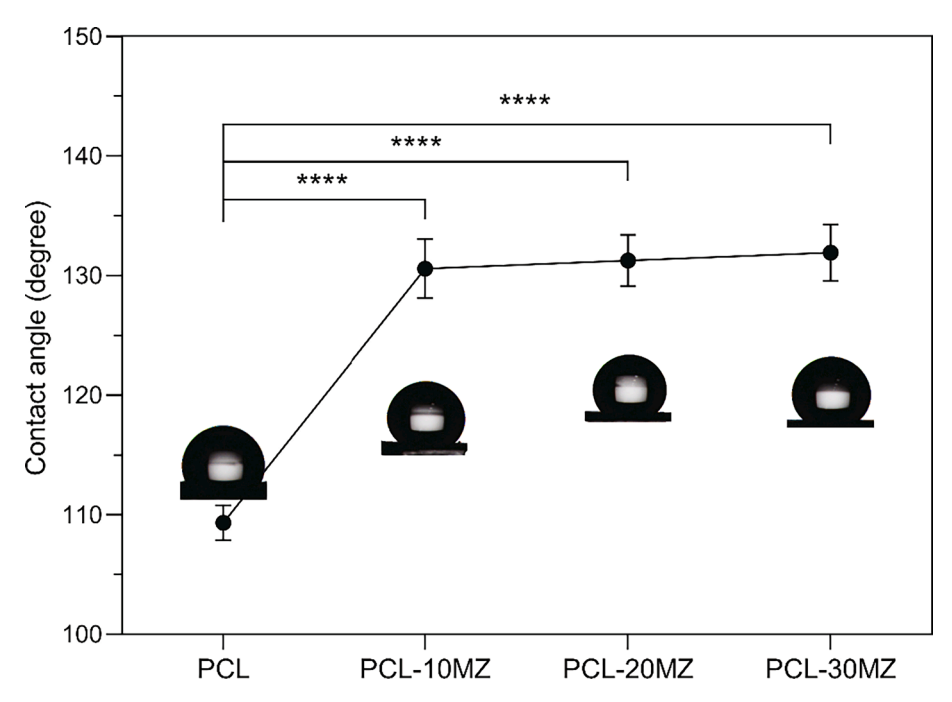


Fig. 10. Water contact angle measurements of PCL, PCL-10MZ, PCL-20MZ, and PCL-30MZ. The error bars indicate means  $\pm$  SD (n=3): \*p<0.05, \*\*p<0.01, \*\*\*\*p<0.001, \*\*\*\*p<0.0001.

biodegradable nanofibrous membrane by electrospinning. The MoS<sub>2</sub>/ZnS heterojunctions inhibited the recombination of photogenerated electron-hole pairs and promoted charge transfer. The incorporation of MoS<sub>2</sub>/ZnS heterojunctions improved the hydrophobicity of PCL and effectively killed bacteria through the synergistic effects of PDT and PTT by exploiting hyperthermia and ROS. The PCL-30MZ nanofibers showed an antibacterial efficiency of 96.03% and 99.09% against *S. aureus* and *E. coli* after 10 min of light irradiation. The biocompatibility of PCL endowed PCL-30MZ nanofibers biosafety without obvious toxicity to cells. Therefore, PCL-30MZ hybrid nanofibers have great potential in the wearable antibacterial fabric.

#### 5. Data availability

The raw/processed data required to reproduce these findings cannot be shared at this time due to technical or time limitations. Data are available upon reasonable request in the future.

#### **Declaration of Competing Interest**

The authors declare that they have no known competing financial interests or personal relationships that could have appeared to influence the work reported in this paper.

# Acknowledgments

This work is jointly supported by the National Natural Science Foundation of China (Nos. 51871162, and 52173251), and the China National Funds for Distinguished Young Scientists (No.51925104).

# Appendix A. Supplementary data

Supplementary data to this article can be found online at  $\frac{\text{https:}}{\text{doi.}}$  org/10.1016/j.cej.2022.134764.

# References

[1] Z. Fan, B. Liu, J. Wang, S. Zhang, Q. Lin, P. Gong, L. Ma, S. Yang, A novel wound dressing based on Ag/graphene polymer hydrogel: effectively kill bacteria and

- accelerate wound healing, Adv. Funct. Mater. 24 (25) (2014) 3933–3943, https://doi.org/10.1002/adfm.201304202.
- [2] https://www.worldometers.info/coronavirus/, (2021, November 18).
- [3] J. Lin, X. Chen, C. Chen, J. Hu, C. Zhou, X. Cai, W. Wang, C. Zheng, P. Zhang, J. Cheng, Z. Guo, H.u. Liu, Durably antibacterial and bacterially anti-adhesive cotton fabrics coated by cationic fluorinated polymers, ACS Appl. Mater. Interfaces 10 (7) (2018) 6124–6136, https://doi.org/10.1021/acsami.7b1623510.1021/acsami.7b16235 s001
- [4] Q. Xu, W. Zheng, P. Duan, J. Chen, Y. Zhang, F. Fu, H. Diao, X. Liu, One-pot fabrication of durable antibacterial cotton fabric coated with silver nanoparticles via carboxymethyl chitosan as a binder and stabilizer, Carbohydr. Polym. 204 (2019) 42–49, https://doi.org/10.1016/j.carbpol.2018.09.089.
- [5] Z. Qin, Y. Zheng, Y. Wang, T. Du, C. Li, X. Wang, H. Jiang, Versatile roles of silver in Ag-based nanoalloys for antibacterial applications, Coord. Chem. Rev. 449 (2021) 214218, https://doi.org/10.1016/j.ccr.2021.214218.
- [6] X. Deng, A. Yu Nikiforov, T. Coenye, P. Cools, G. Aziz, R. Morent, N. De Geyter, C. Leys, Antimicrobial nano-silver non-woven polyethylene terephthalate fabric via an atmospheric pressure plasma deposition process, Sci. Rep. 5 (2015) 10138, https://doi.org/10.1038/srep10138.
- [7] X. He, D. Yang, X. Zhang, M. Liu, Z. Kang, C. Lin, N. Jia, R. Luque, Waste eggshell membrane-templated CuO-ZnO nanocomposites with enhanced adsorption, catalysis and antibacterial properties for water purification, Chem. Eng. J. 369 (2019) 621–633, https://doi.org/10.1016/j.cej.2019.03.047.
- [8] S.M. Botsa, K. Basavaiah, Fabrication of multifunctional TANI/Cu<sub>2</sub>O/Ag nanocomposite for environmental abatement, Sci. Rep. 10 (2020) 14080, https://doi.org/10.1038/s41598-020-70194-9.
- [9] Z. Zhong, Z. Xu, T. Sheng, J. Yao, W. Xing, Y. Wang, Unusual air filters with ultrahigh efficiency and antibacterial functionality enabled by ZnO nanorods, ACS Appl. Mater. Interfaces 7 (38) (2015) 21538–21544, https://doi.org/10.1021/ acsami.5b06810.
- [10] X. Zhang, X. He, Z. Kang, M. Cui, D.-P. Yang, R. Luque, Waste eggshell-derived dual-functional CuO/ZnO/eggshell nanocomposites: (photo)catalytic reduction and bacterial inactivation, ACS Sustainable Chem. Eng. 7 (18) (2019) 15762–15771, https://doi.org/10.1021/acssuschemeng.9b0408310.1021/ acssuschemeng.9b04083.s001.
- [11] Z. Ye, S. Li, S. Zhao, L. Deng, J. Zhang, A. Dong, Textile coatings configured by double-nanoparticles to optimally couple superhydrophobic and antibacterial properties, Chem. Eng. J. 420 (2021) 127680, https://doi.org/10.1016/j. coi.2020.127680
- [12] C. Liu, Y. Guo, X. Wei, C. Wang, M. Qu, D.W. Schubert, C. Zhang, An outstanding antichlorine and antibacterial membrane with quaternary ammonium salts of alkenes via in situ polymerization for textile wastewater treatment, Chem. Eng. J. 384 (2020) 123306, https://doi.org/10.1016/j.cej.2019.123306.
- [13] A.-M. Gavrila, A. Zaharia, L. Paruch, F.X. Perrin, A. Sarbu, A.G. Olaru, A.M. Paruch, T.-V. Iordache, Molecularly imprinted films and quaternary ammonium-functionalized microparticles working in tandem against pathogenic bacteria in wastewaters, J. Hazard. Mater. 399 (2020) 123026, https://doi.org/10.1016/j.jhazmat.2020.123026.
- [14] Y. Liu, J. Li, L. Li, S. McFarland, X. Ren, O. Acevedo, T.S. Huang, Characterization and mechanism for the protection of photolytic decomposition of N-Halamine

- siloxane coatings by titanium dioxide, ACS Appl. Mater. Interfaces 8 (5) (2016) 3516–3523, https://doi.org/10.1021/acsami.5b1260110.1021/acsami.5b12601.
- [15] S. Wu, J. Xu, L. Zou, S. Luo, R. Yao, B. Zheng, G. Liang, D. Wu, Y. Li, Long-lasting renewable antibacterial porous polymeric coatings enable titanium biomaterials to prevent and treat peri-implant infection, Nat. Commun. 12 (2021) 3303, https:// doi.org/10.1038/e41467-021-23069-0
- [16] J. Feng, E. Hontañón, M. Blanes, J. Meyer, X. Guo, L. Santos, L. Paltrinieri, N. Ramlawi, L.C.P.M.d. Smet, H. Nirschl, F.E. Kruis, A. Schmidt-Ott, G. Biskos, Scalable and environmentally benign process for smart textile nanofinishing, ACS Appl, Mater. Interfaces 8 8 (23) (2016) 14756–14765, https://doi.org/10.1021/ acsami.6b0363210.1021/acsami.6b03632.s001.
- [17] B. Li, X. Xia, M. Guo, Y. Jiang, Y. Li, Z. Zhang, S. Liu, H. Li, C. Liang, H. Wang, Biological and antibacterial properties of the micro-nanostructured hydroxyapatite/chitosan coating on titanium, Sci. Rep. 9 (2019) 14052, https://doi.org/10.1038/s41598-019-49941-0.
- [18] S. Foorginezhad, M.M. Zerafat, Fabrication of stable fluorine-free superhydrophobic fabrics for anti-adhesion and self-cleaning properties, Appl. Surf. Sci. 464 (2019) 458–471, https://doi.org/10.1016/j.apsusc.2018.09.058.
- [19] Y. Xu, W. Wen, J.M. Wu, Titania nanowires functionalized polyester fabrics with enhanced photocatalytic and antibacterial performances, J. Hazard. Mater. 343 (2018) 285–297, https://doi.org/10.1016/j.jhazmat.2017.09.044.
- [20] A. Opitakorn, M. Rauytanapanit, R. Waditee-Sirisattha, T. Praneenararat, Non-leaching antibacterial cotton fabrics based on lipidated peptides, RSC Adv. 7 (54) (2017) 34267–34275, https://doi.org/10.1039/C7RA03565A.
- [21] C. Kang, S. Kim, S. Kim, J. Lee, J.H. Lee, C. Roh, J. Lee, Antibacterial cotton fibers treated with silver nanoparticles and quaternary ammonium salts, Carbohydr. Polym. 151 (2016) 1012–1018, https://doi.org/10.1016/j.carbpol.2016.06.043.
- [22] W. Guan, L. Tan, X. Liu, Z. Cui, Y. Zheng, K.W.K. Yeung, D. Zheng, Y. Liang, Z. Li, S. Zhu, X. Wang, S. Wu, Ultrasonic interfacial engineering of red phosphorous–metal for eradicating MRSA infection effectively, Adv. Mater. 33 (5) (2021) 2006047, https://doi.org/10.1002/adma.202006047.
- [23] K. Su, L. Tan, X. Liu, Z. Cui, Y. Zheng, B.o. Li, Y. Han, Z. Li, S. Zhu, Y. Liang, X. Feng, X. Wang, S. Wu, Rapid photo-sonotherapy for clinical treatment of bacterial infected bone implants by creating oxygen deficiency using sulfur doping, ACS Nano 14 (2) (2020) 2077–2089, https://doi.org/10.1021/acsnano.9b0868610.1021/acsnano.9b08686.001.
- [24] S. Wei, Y. Qiao, Z. Wu, X. Liu, Y. Li, Z. Cui, C. Li, Y. Zheng, Y. Liang, Z. Li, S. Zhu, H. Wang, X. Wang, R. Che, S. Wu, Na<sup>+</sup> inserted metal-organic framework for rapid therapy of bacteria-infected osteomyelitis through microwave strengthened Fenton reaction and thermal effects, Nano Today 37 (2021) 101090, https://doi.org/10.1016/j.nantod.2021.101090.
- [25] Y. Qiao, X. Liu, B. Li, Y. Han, Y. Zheng, K.W.K. Yeung, C. Li, Z. Cui, Y. Liang, Z. Li, S. Zhu, X. Wang, S. Wu, Treatment of MRSA-infected osteomyelitis using bacterial capturing, magnetically targeted composites with microwave-assisted bacterial killing, Nat. Commun. 11 (2020) 4446, https://doi.org/10.1038/s41467-020-12036.
- [26] J. Fu, Y. Li, Y.u. Zhang, Y. Liang, Y. Zheng, Z. Li, S. Zhu, C. Li, Z. Cui, S. Wu, An engineered pseudo-macrophage for rapid treatment of bacteria-infected osteomyelitis via microwave-excited anti-infection and immunoregulation, Adv. Mater. 33 (41) (2021) 2102926, https://doi.org/10.1002/adma.202102926.
- [27] Q. Zheng, X. Liu, Y. Zheng, K.W.K. Yeung, Z. Cui, Y. Liang, Z. Li, S. Zhu, X. Wang, S. Wu, The recent progress on metal-organic frameworks for phototherapy, Chem. Soc. Rev. 50 (8) (2021) 5086–5125, https://doi.org/10.1039/D1CS00056J.
- [28] X. Kong, X. Liu, Y. Zheng, P.K. Chu, Y.u. Zhang, S. Wu, Graphitic carbon nitride-based materials for photocatalytic antibacterial application, Mater. Sci. Eng. R-Rep. 145 (2021) 100610, https://doi.org/10.1016/j.mser.2021.100610.
  [29] Y. Ren, H. Liu, X. Liu, Y. Zheng, Z. Li, C. Li, K.W.K. Yeung, S. Zhu, Y. Liang, Z. Cui,
- [29] Y. Ren, H. Liu, X. Liu, Y. Zheng, Z. Li, C. Li, K.W.K. Yeung, S. Zhu, Y. Liang, Z. Cui, S. Wu, Photoresponsive materials for antibacterial applications, Cell Rep. Phys. Sci. 1 (11) (2020) 100245, https://doi.org/10.1016/j.xcrp.2020.100245.
- [30] S. Ning, H. Lin, Y. Tong, X. Zhang, Q. Lin, Y. Zhang, J. Long, X. Wang, Dual couples Bi metal depositing and Ag@AgI islanding on BiOI 3D architectures for synergistic bactericidal mechanism of E. coli under visible light, Appl. Catal. B. 204 (2017) 1–10, https://doi.org/10.1016/j.apcatb.2016.11.006.
- [31] Y. Zhang, C. Lin, Q. Lin, Y. Jin, Y. Wang, Z. Zhang, H. Lin, J. Long, X. Wang, Cul-BiOI/Cu film for enhanced photo-induced charge separation and visible-light antibacterial activity, Appl. Catal. B. 235 (2018) 238–245, https://doi.org/10.1016/j.apcatb.2018.05.001.
- [32] Y. Jin, J. Long, X.i. Ma, T. Zhou, Z. Zhang, H. Lin, J. Long, X. Wang, Synthesis of caged Iodine-modified ZnO nanomaterials and study on their visible light photocatalytic antibacterial properties, Appl. Catal. B. 256 (2019) 117873, https:// doi.org/10.1016/j.apcatb.2019.117873.
- [33] C. Liu, D. Kong, P.-C. Hsu, H. Yuan, H.-W. Lee, Y. Liu, H. Wang, S. Wang, K. Yan, D. Lin, P.A. Maraccini, K.M. Parker, A.B. Boehm, Y.i. Cui, Rapid water disinfection using vertically aligned MoS<sub>2</sub> nanofilms and visible light, Nat. Nanotechnol. 11 (12) (2016) 1098–1104, https://doi.org/10.1038/nnano.2016.138.
- [34] Y. Luo, J. Li, X. Liu, L. Tan, Z. Cui, X. Feng, X. Yang, Y. Liang, Z. Li, S. Zhu, Y. Zheng, K.W.K. Yeung, C. Yang, X. Wang, S. Wu, Dual metal–organic framework heterointerface, ACS Central Sci. 5 (9) (2019) 1591–1601, https://doi.org/ 10.1021/acscentsci.9b00639.
- [35] D. Han, Y. Li, X. Liu, K.W.K. Yeung, Y. Zheng, Z. Cui, Y. Liang, Z. Li, S. Zhu, X. Wang, S. Wu, Photothermy-strengthened photocatalytic activity of polydopamine-modified metal-organic frameworks for rapid therapy of bacteria-infected wounds, J. Mater. Sci. Technol. 62 (2021) 83–95, https://doi.org/10.1016/j.jmst.2020.05.055.

- [36] H.Y. Liu, C.G. Niu, H. Guo, C. Liang, D.W. Huang, L. Zhang, Y.Y. Yang, L. Li, In suit constructing 2D/1D MgIn<sub>2</sub>S<sub>4</sub>/CdS heterojunction system with enhanced photocatalytic activity towards treatment of wastewater and H<sub>2</sub> production, J. Colloid Interface Sci. 576 (2020) 264–279, https://doi.org/10.1016/j.icis.2020.05.025
- [37] D. Xia, Y. Li, G. Huang, C.C. Fong, T. An, G. Li, H.Y. Yip, H. Zhao, A. Lu, P.K. Wong, Visible-light-driven inactivation of *Escherichia coli* K-12 over thermal treated natural pyrrhotite, Appl. Catal. B. 176–177 (2015) 749–756, https://doi.org/ 10.1016/j.apcatb.2015.04.024.
- [38] Y.-Y. Yang, X.-G. Zhang, C.-G. Niu, H.-P. Feng, P.-Z. Qin, H. Guo, C. Liang, L. Zhang, H.-Y. Liu, L.u. Li, Dual-channel charges transfer strategy with synergistic effect of Z-scheme heterojunction and LSPR effect for enhanced quasi-full-spectrum photocatalytic bacterial inactivation: new insight into interfacial charge transfer and molecular oxygen activation, Appl. Catal. B. 264 (2020) 118465, https://doi. org/10.1016/j.apcatb.2019.118465.
- [39] L.u. Li, C.-G. Niu, H. Guo, J. Wang, M. Ruan, L. Zhang, C. Liang, H.-Y. Liu, Y.-Y. Yang, Efficient degradation of Levofloxacin with magnetically separable ZnFe<sub>2</sub>O<sub>4</sub>/NCDs/Ag<sub>2</sub>CO<sub>3</sub> Z-scheme heterojunction photocatalyst: Vis-NIR light response ability and mechanism insight, Chem. Eng. J. 383 (2020) 123192, https://doi.org/10.1016/j.cej.2019.123192.
- [40] Y. Qu, T. Wei, J. Zhao, S. Jiang, P. Yang, Q. Yu, H. Chen, Regenerable smart antibacterial surfaces: full removal of killed bacteria via a sequential degradable layer, J. Mater. Chem. B. 6 (23) (2018) 3946–3955, https://doi.org/10.1039/ CSTR011228
- [41] D. Hu, H. Li, B. Wang, Z. Ye, W. Lei, F. Jia, Q. Jin, K.F. Ren, J. Ji, Surface-adaptive gold nanoparticles with effective adherence and enhanced photothermal ablation of methicillin-resistant staphylococcus aureus biofilm, ACS Nano 11 (2017) 9330–9339, https://doi.org/10.1039/c8tb01122b.
- [42] G.J. Lee, J.J. Wu, Recent developments in ZnS photocatalysts from synthesis to photocatalytic applications — A review, Powder Technol. 318 (2017) 8–22, https://doi.org/10.1016/j.powtec.2017.05.022.
- [43] W. Yin, J. Yu, F. Lv, L. Yan, L.R. Zheng, Z. Gu, Y. Zhao, Functionalized nano-MoS<sub>2</sub> with peroxidase catalytic and near-infrared photothermal activities for safe and synergetic wound antibacterial applications, ACS Nano 10 (12) (2016) 11000–11011, https://doi.org/10.1021/acsnano.6b05810.s001.
- [44] S.E. Kim, Y.P. Yun, K.S. Shim, H.J. Kim, K. Park, H.R. Song, 3D printed alendronate-releasing poly(e-caprolactone) porous scaffolds enhance osteogenic differentiation and bone formation in rat tibial defects, Biomed. Mater. 11 (2016), 055005, https://doi.org/10.1088/1748-6041/11/5/055005.
- [45] A.J. Reid, A.C. de Luca, A. Faroni, S. Downes, M. Sun, G. Terenghi, P.J. Kingham, Long term peripheral nerve regeneration using a novel PCL nerve conduit, Neurosci. Lett. 544 (2013) 125–130, https://doi.org/10.1016/j. neulet.2013.04.001.
- [46] B.-K. Lee, Y.M. Ju, J.-G. Cho, J.D. Jackson, S.J. Lee, A. Atala, J.J. Yoo, End-to-side neurorrhaphy using an electrospun PCL/collagen nerve conduit for complex peripheral motor nerve regeneration, Biomaterials 33 (35) (2012) 9027–9036, https://doi.org/10.1016/j.biomaterials.2012.09.008.
- [47] M. Sun, P.J. Kingham, A.J. Reid, S.J. Armstrong, G. Terenghi, S. Downes, *In vitro* and *in vivo* testing of novel ultrathin PCL and PCL/PLA blend films as peripheral nerve conduit, J. Biomed. Mater. Res. Part A. 93 (2010) 1470–1481, https://doi.org/10.1002/jbm.a.32681.
- [48] N.K. Singh, S.K. Singh, D. Dash, B.P. Das Purkayastha, J.K. Roy, P. Maiti, Nanostructure controlled anti-cancer drug delivery using poly(e-caprolactone) based nanohybrids, J. Mater. Chem. 22 (2012) 17853–17863, https://doi.org/ 10.1039/C2JM32340K.
- [49] K. Ghosal, A. Chandra, P. G., S. S., S. Roy, C. Agatemor, S. Thomas, I. Provaznik, Electrospinning over solvent casting: tuning of mechanical properties of membranes, Sci. Rep. 8 (1) (2018), https://doi.org/10.1038/s41598-018-23378-3.
- [50] L. Sun, L. Song, X.u. Zhang, R. Zhou, J. Yin, S. Luan, Poly(γ-glutamic acid)-based electrospun nanofibrous mats with photodynamic therapy for effectively combating wound infection, Mater. Sci. Eng. C. 113 (2020) 110936, https://doi. org/10.1016/j.msec.2020.110936.
- [51] G.Z. Yang, J.J. Li, D.G. Yu, M.F. He, J.H. Yang, G.R. Williams, Nanosized sustained-release drug depots fabricated using modified triaxial electrospinning, Acta Biomater. 53 (2017) 233–241, https://doi.org/10.1016/j.actbio.2017.01.069.
- [52] X. Hu, S. Liu, G. Zhou, Y. Huang, Z. Xie, X. Jing, Electrospinning of polymeric nanofibers for drug delivery applications, J. Controlled Release. 185 (2014) 12–21, https://doi.org/10.1016/j.jconrel.2014.04.018.
- https://doi.org/10.1016/j.jconrel.2014.04.018.
  [53] X. Wang, L. Dou, L. Yang, J. Yu, B. Ding, Hierarchical structured MnO<sub>2</sub>@SiO<sub>2</sub> nanofibrous membranes with superb flexibility and enhanced catalytic pe, J. Hazard. Mater. 324 (2017) 203–212, https://doi.org/10.1016/j.jhazmat.2016.10.050.
- [54] Y.i. Shi, Y. Zhou, D.-R. Yang, W.-X. Xu, C. Wang, F.-B. Wang, J.-J. Xu, X.-H. Xia, H.-Y. Chen, Energy level engineering of MoS<sub>2</sub> by transition-metal doping for accelerating hydrogen evolution reaction, J. Am. Chem. Soc. 139 (43) (2017) 15479–15485, https://doi.org/10.1021/jacs.7b0888110.1021/jacs.7b08881.s001.
- [55] S. Chen, Y. Hu, S. Meng, X. Fu, Study on the separation mechanisms of photogenerated electrons and holes for composite photocatalysts g-C<sub>3</sub>N<sub>4</sub>-WO<sub>3</sub>, Appl. Catal. B. 150–151 (2014) 564–573, https://doi.org/10.1016/j. aprath 2013 12 053
- [56] S. Kumar, N.L. Reddy, H.S. Kushwaha, A. Kumar, M.V. Shankar, K. Bhattacharyya, A. Halder, V. Krishnan, Efficient electron transfer across a ZnO–MoS<sub>2</sub>–reduced graphene oxide heterojunction for enhanced sunlight-driven photocatalytic hydrogen evolution, ChemSusChem 10 (18) (2017) 3588–3603, https://doi.org/ 10.1002/cssc.201701024.

- [57] Y.-Y. Yang, H.-P. Feng, C.-G. Niu, D.-W. Huang, H. Guo, C. Liang, H.-Y. Liu, S. Chen, N. Tang, L.u. Li, Constructing a plasma-based Schottky heterojunction for near-infrared-driven photothermal synergistic water disinfection: Synergetic effects and antibacterial mechanisms, Chem. Eng. J. 426 (2021) 131902, https:// doi.org/10.1016/j.cej.2021.131902.
- [58] Y. Wang, Y. Liu, Y. Qian, L. Lv, X. Li, Y. Liu, Characteristics of MgO/PCL/PVP antibacterial nanofiber membranes produced by electrospinning technology, Surf. Interfaces. 28 (2022) 101661, https://doi.org/10.1016/j.surfin.2021.101661.
- [59] Y. Ghiyasi, E. Salahi, H. Esfahani, Synergy effect of Urtica dioica and ZnO NPs on microstructure, antibacterial activity and cytotoxicity of electrospun PCL scaffold for wound dressing application, Mater. Today Commun. 26 (2021) 102163, https://doi.org/10.1016/j.mtcomm.2021.102163.
- [60] B. Liu, T. Yao, L. Ren, Y. Zhao, X. Yuan, Antibacterial PCL electrospun membranes containing synthetic polypeptides for biomedical purposes, Colloids Surf. B 172 (2018) 330–337, https://doi.org/10.1016/j.colsurfb.2018.08.055.